Comparative in-vitro study of contact and image-based rigid registration for computer-aided surgery

Ofri Sadowsky, Ziv Yaniv, and Leo Joskowicz

Computer-Aided Surgery and Medical Image Processing Laboratory
School of Computer Science and Engineering
The Hebrew University of Jerusalem, Jerusalem 91904, Israel

Email: josko@cs.huji.ac.il

Abstract

We present an in-vitro study of rigid registration methods for computer-aided surgery. The goal of the study is to empirically obtain accuracy measures under optimal laboratory conditions and to identify the weak links in the registration chain. Specifically, we investigate two common registration methods: contact-based registration and image-based landmark registration. We establish a framework for comparing the accuracy of both methods and describe phantoms, protocols, and algorithms for tool tip calibration, contact-based registration with an optical tracker, fluoroscopic X-ray camera calibration, and fluoroscopic X-ray image-based landmark registration. We report an average accuracy of 0.5mm (1.5mm maximum) and 2.75mm (3.4mm maximum) for contact-based and image-based landmark registration, respectively. Based on our findings, we identify the camera calibration as being the main source of error in image-based landmark registration. We propose protocol improvements and algorithmic refinements to improve the accuracy of image-based landmark registration.

Keywords: registration, image-based registration, contact-based registration, accuracy measurements, fluoroscopy, tracking

Introduction

Registration is the task of finding a transformation from the coordinate system of one modality data set to another so that all features that appear in one modality are aligned with their appearance in the second. Registration is an essential step in most computer-aided surgery (CAS) systems, since it is necessary to match information from different data modalities obtained at different points in time. It is required to match the preoperative images and plans to the intraoperative situation, and to determine the relative positions of surgical tools and anatomical structures. Examples of deployed CAS systems include preoperative planning, intraoperative navigation, and robotic s systems for orthopaedic surgery [1-4], neurosurgery [5,6], and maxillofacial surgery [7], among many others. Practical, accurate, and robust registration has emerged as one of the key technical challenges in the field [3]. Much recent research has been devoted to the development and validation of registration methods (see [8] for an excellent survey).

This paper presents an in-vitro study of rigid registration methods for computer-aided surgery. The purpose of the study is to empirically obtain accuracy measures under optimal laboratory conditions and to identify the weak links in the registration chain. While the setup is different from the one used clinically, the study aims at obtaining a lower bound on the achievable accuracy and at identifying the main sources of error. Establishing the accuracy and robustness of the registration methods is essential for determining their potential applicability in different clinical settings. Understanding of the factors that affect the accuracy and robustness of the registration process provides quantitative criteria to support the selection of registration methods, and indicates where technical improvements are necessary.

We address the rigid registration of the preoperative three-dimensional (3D) model of an object with its intraoperative pose. This type of registration is very common in orthopaedics, where mesh models of bone structures are constructed preoperatively from CT scans, and a surgical plan, consisting of landmark points, axes, or implants, is elaborated based on the images and the models. The plan has then to be registered to the intraoperative situation so that it can be carried out precisely with the help of a navigation system or a robotic device. The registration is usually performed with an instrumented pointer touching implanted fiducials, anatomical landmarks, or points on the surface of the anatomy to get their precise spatial locations. The points are then matched with the corresponding points in the 3D model to obtain the three rotation and three translation parameters of the rigid transformation that achieves the best coincidence between them. This procedure is also used to register nearly rigid structures, such as brain structures in neurosurgery, in which adhesive fiducials are placed on the patient's forehead [9].

While effective and accurate, contact-based rigid registration methods have two main drawbacks: they require part of the anatomy of interest to be exposed, and they can be time-consuming and error-prone. Intraoperative exposure of all or part of the anatomy of interest so it can be touched with a pointer can result in additional undesired surgical incisions. In percutaneous procedures, such as needle insertion or long bone closed fracture reduction, the additional surgical incisions defeat the purpose of the minimally invasive procedure. The additional incisions can also be necessary in some more invasive procedures, such as in pelvic fracture reduction, to obtain the desired accuracy with an even distribution of points on the anatomical structure. It is only practical to acquire a few dozen points, since each acquisition is time-consuming. Additional errors are also introduced with the presence of tissue and fat on the anatomical surface.

An alternative to contact-based registration is image-based registration. In image-based registration, one or more intraoperative images of the anatomy of interest are acquired at known camera poses. Feature points, such as fiducial centers, anatomical landmarks, or anatomical contours, are extracted from the images, and their spatial locations are computed from the camera pose and internal parameters. The most commonly used intraoperative imaging devices are mobile fluoroscopic X-ray C-arms and ultrasound units. The advantage of image-based registration is that it does not require contact or additional surgical exposure and uses readily available intraoperative imaging devices. It has the potential to be faster and more stable than contact-based registration, since many points can be extracted accurately and automatically with advanced image processing techniques. However, image-based registration is technically much more challenging, since it depends on many more factors than contact-based registration: the geometric characteristics of the imaging camera and its pose, the image quality, and the quality of feature localization in the images.

This study establishes a technical framework to compare the accuracy of both contact-based and image-based landmark registration methods [10-11]. Specifically, we focus on registration using an optical tracker and fluoroscopic X-ray images obtained by common mobile intraoperative C-arm units. To this end, we developed phantoms, protocols, and algorithms for tool tip calibration, contact-based registration, fluoroscopic X-ray camera distortion correction and calibration, and fluoroscopic X-ray image-based landmark registration. We designed and conducted in-vitro experiments to test the accuracy and reliability of algorithms and protocols under optimal conditions. The individual steps of the registration algorithms are evaluated independently and lower bounds are established.

Previous work

This section reviews previous work on contact and image-based rigid registration methods, and theoretical and experimental accuracy studies.

Contact-based registration methods are currently in use in many commercial systems. These methods match the actual location of implanted fiducials, anatomical landmarks, or points on the surface of the anatomy (a cloud of points) to the corresponding points in the preoperative model. The rigid transformation for fiducial and landmark-based registration is obtained directly with Horn's closed form solution [12], or iteratively by distance minimization [13]. Cloud-of-points registration is performed with the Iterative Closest Point (ICP) method [14]. Several studies report millimetric accuracy in clinical settings for contact-based registration [6,15-19,21].

Several image-based registration methods have been proposed recently, although no commercial system, with the exception of the CyberKnife™ system for radiation therapy of brain tumors [20], uses them. The registration can be based on geometric features in the image [22-26] or on pixel intensity values [27-32]. Geometric registration requires feature segmentation (e.g., fiducial center location, contour edge detection), while intensity-based registration requires generating digitally reconstructed radiographic images and comparing them with the actual fluoroscopic X-ray images. The main difficulty with geometric registration is the accuracy and robustness of feature segmentation. The main difficulty of intensity-based registration is the size of the search space and the existence of many local minima. Several groups have reported millimetric accuracy for image-based registration. Lavallée and Hamadeh [23,25] report an in-vitro accuracy of 2mm on a dry vertebra. Tang [26] reports an in-vitro accuracy of 3mm on long bone foam models with six metal fiducials and a single image. Larose [27] reports an in-vitro accuracy of 1.3mm on a 60x60x60 mm^3 phantom.

A necessary first step for image-based registration is to obtain an accurate model of the imaging process. The camera has to be calibrated and the image corrected for distortion. Much recent work, including our own [10,33] has been devoted to fluoroscopic X-ray image distortion correction [2,26,34,35] and pinhole camera calibration [36, 37].

Several theoretical studies on the accuracy of rigid registration have been conducted. Fitzpatrick and West [38,39,40] analyze the target registration error (TRE), which is defined as the error between the measured and expected position of a point after the registration as a function of the fiducial localization error. They show that the target registration error does not depend on the initial displacement between the model and the samples, and characterize the dependency of this error's distribution on the spatial configuration of the landmarks or fiducials. Pennec [41] presents a statistical framework for point-based registration where geometric features are described as couples, data (coordinates) and uncertainty (covariance matrix). He describes a rigid registration algorithm, which yields both the motion and its uncertainty and allows the computation of expected error at every object point. Ellis [42] presents a framework for registration stability evaluation, given known localization error bounds in the registered modalities.

Methods

The goal of our study is to establish a common framework that allows a direct comparison of contact and image-based landmark registration methods. This section presents the generic registration algorithm and a brief review of the algorithms that we use in our study (for full details, see [11]).

The registration process consists of five steps:

1. Calibration: calibrate the data acquisition devices (optical tracker, fluoroscopic X-ray C-arm) and correct for distortions.

2. Feature extraction: find features in both data sets, such that a feature in one set can be matched with a corresponding feature in the other.

3. Feature pairing: match the corresponding features in both data sets. Eliminate outlier pairings.

4. Similarity formulation: define a disparity function, which is a global similarity measure between the two data sets, based on the pairings.

5. Dissimilarity reduction: reduce the dissimilarity between the two data sets by minimizing the disparity function.

Steps 2-5 are repeated until convergence is reached.

Contact-based registration method

Contact-based registration consists of matching two 3D point sets. Since the point sets are given, no feature extraction is necessary. When using fiducials or landmarks, the pairing is known since it is determined aprori from the point acquisition protocol. The similarity measure between the data sets is the sum of the squared distances between pairs of points in both data sets. We use Horn's closed form solution [12] for point-based registration, and the Iterative Closest Point (ICP) method [14] for cloud-of-points registration. Each sample point is iteratively matched with its nearest neighbor in the model set, and then a transformation that minimizes the distance between them is computed using Horn's formula. The algorithm is guaranteed to reach a local minimum, which is also the right one when the initial pose estimate is close enough (for example, one obtained by approximate landmark).

For contact-based registration, the optical tracker and tool must be calibrated. The tracker does not require calibration since it comes pre-calibrated from the factory. We calibrate the tool to determine the exact position of the tool tip with a custom calibration algorithm based on the CalTrax™ calibration tool (Traxtal Technologies, Toronto, Canada) shown in Figure 1. The algorithm derives the position of the tool tip from the geometry and position of the tracked pointer and the calibration tool. The geometry is determined by the diameter of the tool and the geometric characteristics of the calibration tool.

Image-based landmark registration method

Image-based landmark registration consists of matching a set of 3D points (the model) with a set of 2D points extracted from the images, in our case fiducials.

A prerequisite for fluoroscopic X-ray image-based registration is image distortion correction and calibration, for which we use the algorithms described in [33]. The fluoroscopic X-ray C-arm is modeled as a pinhole camera, as this has been shown to be a very good approximation of the X-ray imaging process. We use local bi-linear interpolation on a dense grid of points to compute a distortion map. For camera calibration, we use the pinhole camera calibration algorithm based on constrained optimization described in [36]. It computes the internal camera parameters (focal length, image center, and scaling) and the external parameters corresponding to the camera pose. The algorithm is more robust and reliable than Tsai's method [37], which we used originally, although it is very sensitive to small differences in fiducial centers.

Since we perform image-based landmark registration with a phantom consisting of spherical metal balls as fiducials, the feature extraction and feature pairing steps are straightforward. To extract the fiducial centers to sub-pixel accuracy, we use the circle center Hough transform [43], followed by gray-level thresholding segmentation. The pairing between the model and computed center is then done manually. We minimize the error measure consisting of the sum of distances between the model points and the closest points on the rays emanating from the camera source and passing through the image points.

Materials and protocols

This section describes the equipment, phantoms, and protocol used in our study. The equipment consists of a standard PC computer with a video card and a monitor, a Phillips BV 29 mobile fluoroscopic X-ray (C-arm) unit with a 9" field of view (Amsterdam, The Netherlands), a hybrid optical tracker Polaris ^{TM} (Northern Digital Inc., Ontario, Canada), and tracking instruments from Traxtal Technologies (Toronto, Canada). We use both flat active tracking plates and cross-like optical passive trackers as dynamic reference frames, actively and passively tracked pointers for landmark acquisition, and the CalTrax ^{TM} calibration device for pointer tip calibration (Figure 1). Images are directly downloaded from the fluoroscopic unit to the PC computer via the video output port with the GrabIt Pro II ^{TM} analog to digital frame grabber.

Phantoms

We designed and built four custom phantoms for the in-vitro registration experiments: a dewarp grid, a camera calibration phantom, a contact-based registration phantom, and a four-way registration phantom. With the exception of the dewarp grid, all phantoms have attached to them an active tracking plate that serves as a dynamic reference frame. The holes in the phantoms, which are used as precise landmarks for contact-based registration, are cone shaped, so that the center of a spherical tip pointer inside the hole is invariant with respect to the pointer's orientation.

The dewarp grid is used to correct the images for geometric distortion (Figure 2). It is a 7mm thick coated aluminum alloy plate with 405 4mm diameter holes uniformly distributed on a grid at 10mm intervals machined to 0.02mm precision.

It attaches to the C-arm image intensifier via existing screw holes. This grid is simpler and cheaper to make than the commonly used steel balls or cross hairs mounted on a radiolucent plate. The grid features are sufficiently dense and yield very accurate results [44].

The camera calibration phantom is used to obtain the intrinsic imaging parameters of the fluoroscopic X-ray unit (Figure 3). It is a radiolucent, three-step hexagonal tower, with 13 positional holes drilled into it and 12 steel balls pressed into it with a positional accuracy of +/- 0.05mm. The tower dimensions are 200mm height and 60mm, 100mm, and 140mm external diameters for the upper, middle, and lower steps, respectively. The tower is hollow, with cutout windows on the faces of the middle and upper steps to reduce its weight and increase its radiolucency. It is made out of Delrin^{TM}, weights approximately 1.5kg, and attaches to the C-arm image intensifier via existing screw holes.

The camera calibration phantom was designed to have three reference planes, and to allow for robust and accurate ball center computation. The holes are used for contact-based landmark registration to determine the steel balls positions during the calibration. The steel balls were placed right above the cutout windows, so that their appearance is sharp and contrasted in the fluoroscopic images. The holes and balls placement pattern was designed to avoid radial and mirror symmetry, thus allowing unambiguous automatic pairing. Reducing the weight was important to minimize the C-arm deflection. To verify that our phantom indeed did not affect the C-arm deflection, we attached tracking units on the source and image intensifier and measured their relative position with and without the phantom, in several C-arm orientations. No significant difference was detected between measurements with and without the phantom.

The contact-based registration phantom is used for landmark and cloud-of-points contact registration (Figure 4). It is a two-step hexagonal tower with 31 positional holes whose depth has been measured with a precision of +/- 0.05mm. The tower dimensions are 250mm height and 70mm and 100mm external diameters for the upper and lower level, respectively. The tower is one solid piece of Delrin^{TM} whose dimensions are made to +/-0.025mm accuracy. The holes in the phantom are distributed so as to maximize the number of different distances between them. The surfaces of the object can be used to obtain sampled points from several planes for cloud-of-points contact registration.

The four-way registration phantom can be used for both contact-based landmark and cloud-of-points contact registration, and for landmark image-based and contour image-based registration (Figure 5). It is an L-shaped base with small L-shaped blocks on top of it. It has 11 steel balls pressed into it and 9 positional holes drilled into it with a positional accuracy of +/- 0.05mm. The L-shaped base has length 85mm, width 70mm, and height 40mm, and the small blocks glued to it are 15 x15x15mm^3. The phantom is made out of Delrin^{TM} and was designed to fit in its entirety in the fluoroscopic image.

The holes in the phantom are arranged so as to allow easy identification and to maximize the distances between them. The steel balls are spatially distributed so as to avoid overlaps from a wide range of viewing directions. The surfaces of the object can be used to obtain sampled points from several planes for cloud-of-points contact registration. The object shape can also be used for contour-based registration, which is not described in this paper.

Protocols

We define the following protocols for tool-tip calibration, contact-based registration, fluoroscopic camera distortion correction and calibration, and image-based landmark registration.

For tool-tip calibration, we place the cylindrical body of the tracked pointer on the CalTrax^{TM} groove and push it until the spherical tip touches the unit's calibration wall (Figure 1). From the unit geometry and the tool diameter, we determine directly the tool-tip position.

For contact-based landmark registration, we touch the holes with the calibrated pointer and apply Horn's closed form solution [12]. For contact-based cloud-of-points registration, we first obtain an approximate initial guess touching the holes with the calibrated pointer, adding random error to the measurement, and solving in closed form. Then, we acquire a set of points on the surface of the phantom and apply iterative optimization to obtain the rigid transformation. These methods are applied to all three phantom objects.

For fluoroscopic X-ray camera calibration, we compute the distortion map and the intrinsic camera parameters at predefined C-arm poses. The images used for calibration are acquired with power settings of 48kV and 52kV respectively. The image size is 800x600 pixels and the pixel is 0.44x0.44mm^2 after dewarping. To compute the dewarp map, we attach the dewarp grid to the image intensifier, acquire an image, and transfer it to the computer. The plate is then removed, and the calibration phantom is attached in its place. An active tracking plate is fixed on the calibration phantom, and the registration between this plate and the phantom's steel balls is determined using the contact-based landmark registration method. A second tracking plate is attached to the C-arm's image intensifier, and serves as a dynamic reference frame for the C-arm camera. Figure 3 shows the actual setup for calibration. The algorithm then automatically identifies from the fluoroscopic images the centers of the steel balls, whose diameter is 5-10 pixels to sub-pixel accuracy, and computes the internal camera parameters using Faugeras' camera calibration method [36] (earlier experiments with Tsai's method [37] were not sufficiently robust). Figure 6 shows the registration chain for the camera calibration protocol.

For image-based landmark registration, we use the four-way calibration object. We place the four-way calibration object on a radiolucent table whose height is roughly where the patient lies, and take images from the predetermined poses. After automatically identifying the steel balls centers in each image with the same method as above, we manually pair their centers with those of the model and compute the transformation.

Experimental results

We designed and conducted experiments to determine the accuracy of the tracking system, contact-based landmark and cloud-of-points registration, camera calibration, and image-based landmark registration.

Tracking system

To establish a ground truth basis for the tracker, we estimated the positioning accuracy for a static tool using the Polaris tracking system. The magnitude of this noise defines a limit on the accuracy of all other measurements performed with the system. We placed two calibrated tools on a table and recorded 15,000 samples of their coordinate frames and tool tips. We obtained a deviation of the tools' distance from the tracker's origin in the range of 0.13-0.18mm, and 0.11-0.21mm for the tool tips. The larger deviation accounts for the amplification of the tool orientation by the distance along the tools axis. The largest deviation is along the optical axis of the tracker camera.

Contact-based landmark registration accuracy

The goal of this experiment is to measure the accuracy of the contact-based landmark registration method and to determine if there is a significant improvement when more than five landmark points are used. To this end, we selected five spatially distributed holes on the contact registration phantom, touched them with the pointer to acquire their positions, and computed from them the registration matrix. Then, we compared the expected position of all 31 holes, including those used for the registration, with the computed ones and averaged the difference to obtain the target registration error. We repeated the experiment with ten landmarks, four times each.

Table 1 summarizes the results. We conclude that our tool calibration and fiducial registration algorithm result in sub-millimetric accuracy, with a mean of 0.55mm and standard deviation of 0.22mm with five fiducials, and a mean of 0.51mm and standard deviation of 0.29mm with ten fiducials. Note that the improvement from five to ten landmarks is relatively small and does not provide a real advantage. This is probably because the results obtained with only five fiducials are already near optimal when considering the error bounds of the tracking system.

Contact-based cloud-of-points registration accuracy

The goal of this experiment is to measure the accuracy of the cloud-of-points contact registration and its sensitivity to the initial guess computed from approximate landmarks. We use the contact-based registration phantom as in the previous section. To simulate the position uncertainty of the landmarks, we added a 2.5mm error to the hole depth and acquired three landmark positions in different spatial configurations. We use three landmarks for the initial registration and measure its accuracy as described in the previous section. We then acquire a cloud of 15 points on the surface of the phantom, computed the new registration, and compared the results. We repeated the experiment for three different configurations, as shown in Figure 7.

Table 2 summarizes the results. We note that the landmark configuration affects the bias caused by the added error. In the first configuration, two of the landmarks were selected on opposite walls of the hexagon, and the third on the face between them. This causes cancellation of the error, and therefore the initial error is the smallest. In the second configuration, two landmarks on opposite walls were selected, and the third not between them. In the third configuration, all landmarks are on the same side of the tower, thereby introducing a bias. As expected, this configuration yields the worst results. The average error after the cloud-of-points optimization is 1.26mm, with a standard deviation of 0.68mm. We conclude that the cloud-of-point registration significantly reduces, as expected, the error of the initial guess, but is still dependent on it.

Camera calibration accuracy and sensitivity

The goal of these experiments is to measure the accuracy and sensitivity of the camera calibration process. Prior to the experiments, we calibrate the fluoroscopic camera with the calibration phantom attached to the image intensifier as described above.

The first experiment is designed to estimate the calibration accuracy. For this, we use the calibration phantom and image it from different angles and at different heights. In the first setup, we place the calibration phantom on the image intensifier and image it at predefined camera angles. In the second setup, we place the calibration phantom on a radiolucent table and image it at a fixed camera angle but at different heights by raising and lowering the C-arm. In both cases, we compute the error as the distance between the actual position of the fiducial center (as provided by the tracked position of the phantom and its 3D model) and the back-projected ray emanating from the steel ball center in the image to the camera focal point (whose location is known from its tracked position).

Table 3 summarizes the results. The first three rows are the results for the calibration phantom on the image intensifier at three different camera angles. The fourth is the result of the calibration phantom on the radiolucent table imaged at different camera heights. The fifth row averages these results. The mean error is

0.84mm, with a worst case of 2.64mm. The sixth row shows the residual calibration error computed by taking the same image used for calibration and projecting the ball centers on it after the calibration parameters were computed. Since this residual error is much smaller than the calibration error (0.15mm versus 0.84mm on average), it can be neglected.

The second experiment is designed to evaluate the sensitivity of the calibration parameters to the fiducial center locations in the image. For each image that was used to compute the calibration parameters, we extract the fiducial locations with two different gray-level thresholds. This yields two sets of slightly different fiducial centers, with which two sets of calibration parameters are computed.

Tables 4 and 5 summarize the results. In Table 4, we observe that a variation of 0.23 pixels (0.11mm) can cause variations of up to 10mm in some of the projection parameters. However, since the calibration parameters are not independent of each other, a direct comparison of the individual values is not very meaningful. To assess the effect of all the parameters, we compute for the same images the distance between the known fiducial location centers and the back-projected ray for each set of calibration parameters. The results are summarized in Table 5. We note that despite the fact that the individual parameter changes are large, the mean distance difference is very small (about 0.06mm).

Image-based landmark registration accuracy

The goal of this experiment is to quantify the accuracy of image-based landmark registration with the four-way registration phantom. First, we calibrate the fluoroscopic camera as described before and then take one or more images of the phantom. Using these images, the rigid transformation is then computed from the fiducial centers in the image. We evaluate the accuracy of the resulting transformation in two ways. First, we use the phantom positional holes as the target points and measure the target registration error. Second, we compare the transformation to the "gold standard", which is the transformation obtained by contact-based registration.

Table 6 summarizes the results of the target registration error analysis. We observe that using one AP image produces an error of over 6mm, most of it along the axis orthogonal to the image plane. This suggests that determining the distance of the registered object along the fluoroscopic camera's optical axis is the most difficult part of image based registration. Note that despite the failure of using the lateral fluoroscopic image of the phantom for registration, combining the data from both camera angles using the least squares formulation described in [25] succeed and improved the registration results significantly. Nevertheless, the overall results of the image-based registration are still poor compared to the contact-based methods, with an average distance error of 2.75mm and 3.4mm in the worst case when using images from two angles.

Table 7 summarizes the results of the comparison to the gold standard. We observe that the rotation difference is less than 1.5^{o} around each axis in most cases, and about 1^{o} around each axis in the average case. This difference causes errors of about 2mm when the radius of rotation is 100mm. Note that larger differences appear in the translational part of the transformation, and that these differences are usually reduced when more images are used as input for the registration procedure. This suggests that the error in the calibration results is related to the position of the radiation source more than to the orientation of the image plane.

Discussion

The goal of our experiments was to establish a framework for comparing the accuracy of contact and image-based landmark rigid registration. For this purpose, we developed phantoms and protocols for testing algorithms for tool tip calibration, contact-based registration with an optical tracker, fluoroscopic X-ray camera calibration, and fluoroscopic X-ray image-based landmark registration.

All the experiments were conducted under optimal laboratory conditions, which are not necessarily those of the operating room. The goal was to establish a lower bound on the system accuracy and to identify and quantify the weak links of the registration framework. Understanding of the factors that affect the accuracy and robustness of the registration process provides quantitative criteria to support the selection of registration methods, and indicates where technical improvements are necessary.

We found an average accuracy of 0.5mm (1.5mm maximum) and 2.75mm (3.4mm maximum) for contact-based and image-based landmark registration, respectively. We also found that for contact-based registration five fiducials are enough to produce near optimal results, most likely due to the tracking systems accuracy. While the accuracy of contact-based landmark registration is close to the accuracy of the tracking system, the accuracy decreases with cloud-of-points and image-based landmark registration. We identified the fluoroscopic X-ray camera calibration process as being the main source of error in image-based registration. This is because the projection parameters computed for one fluoroscopic image do not accurately fit the projection of other images taken while the fluoroscope's position remains fixed. Despite the errors in our experimental result, we show that our protocols can be used to compute rigid registration with a millimetric accuracy under optimal conditions.

Conclusion and future work

We have described a methodology and an in-vitro study of two types of rigid registration methods for computer-aided surgery: contact-based and image-based landmark registration. We describe phantoms, protocols, and algorithms for tool tip calibration, contact-based registration with an optical tracker, fluoroscopic X-ray camera calibration, and fluoroscopic X-ray image-based landmark registration. We identify camera calibration as the main source of error in image-based registration. These results indicate that in contrast with contact-based registration, image-based landmark registration requires further improvement before it can be used clinically.

Since we identified that camera calibration is the single most important factor of error in image-based registration, we designed and built a new calibration and tracking ring for the C-arm and have improved the calibration algorithm. Preliminary studies show a two-fold improvement on the accuracy, showing that image-based registration has potential for clinical use. We are currently developing registration algorithms for contour-based registration, which we are validating with dry bones. Plans for future work include in-vivo studies.

Acknowledgment

This research was supported in part by a grant from the Israel Ministry of Industry and Trade for the IZMEL Consortium on Image-Guided Therapy. We thank Neil Glossop from Traxtal Technologies for his advise and support.

Bibliography

[1] DiGioia, A.M, Simon, D.A., Jaramaz, B., Blackwell, M., Morgan F.. O'Toole R.V., and Colgan, B. Hipnav: Preoperative planning and intraoperative navigational guidance for acetabular implant placement in total hip replacement surgery. In L. P. Nolte and R. Ganz, editors, *Computer Assisted Orthopedic Surgery*. Hogrefe and Huber Publishers, 1999.

[2] Hofstetter, R., Slomczykowski, M., Sati M., and Nolte, L. P. Fluoroscopy as an imaging means for computer assisted surgical navigation. *Computer Aided Surgery* **4**(2): 65--76, 1999.

[3] Taylor, R.H. Lavallée, S., Burdea, G., and Mösges, R. *Computer-Integrated Surgery: Technology and Clinical Applications*. MIT Press, 1996.

[4] Joskowicz, L., Milgrom, C., Simkin, A., Tockus, L., and Yaniv, Z. FRACAS: A system for computer-aided image-guided long bone fracture surgery. *Computer Aided Surgery* **3**(6): 271--288, 1998.

[5] Zamorano, L., Matter, A., Saenz, A., Buciuc, R., and Diaz, F. Interactive image-guided resection of cerebral cavernous malformations. *Computer Aided Surgery* **2**(6): 327--332, 1997.

[6] Smith, K., Frank, K.J., and Bucholz, R. The Neurostation: a highly accurate, minimally invasive solution to frameless stereotactic neurosurgery. *Comp. Med. Imag. Graphics* **18**(1): 247--56, 1994.

[7] Hassfled, S., and Mühling, J. Navigation in maxillofacial and craniofacial surgery. *Computer Aided Surgery* **3**(1): 183--187, 1998.

[8] Maintz, J.B.A., and Viergever, M.A. A survey of medical image registration. *Medical Image Analysis* **37**-1(1)2, 1998.

[9] Darabi, K., Grunert, P., and Perneczky, A. Accuracy of intraoperative navigation using skin markers. *Proc. of the 13th Int. Conf on Computer Aided Radiology and Surgery*, In H.U. Lemke et al., editors. Elsevier, pp 920--924, 1997.

[10] Yaniv, Z., Sadowsky, O., and Joskowicz, L. In-vitro accuracy study of contact and image-based registration: Materials, methods, and experimental results. *Proc. of the 15th Int. Conf on Computer Aided Radiology and Surgery*, In H.U. Lemke et al., editors, Elsevier, 2000.

[11] Sadowsky, O. Contact and image-based rigid registration in computer-assisted surgery: materials, methods, and experimental results. Master's Thesis, School of Computer Science and Engineering, The Hebrew University of Jerusalem, 2001.

[12] Horn, B.K.P. Closed-form solution of absolute orientation using unit quaternions. *Journal of the Optical Society of America A* **4**(4): 629—642, 1987.

[13] Lavallée, S. *Registration for computer-integrated surgery: Methodology, state of the art*. In Taylor R.H., Lavallée S., Burdea G.C., and Mösges R., editors, *Computer-integrated surgery*: *Technology and clinical applications*. Chapter 5, pp 77—97, MIT Press, Cambridge MA, 1995.

[14] Besl, P.J., and McKay, N.D. A method for registration of 3D shapes. \e *IEEE Trans. on Pattern Analysis and Machine Intelligence* **14**(2): 239-255, 1992.

[15] Bolger, C., Wigfield, C., Melkent, T., and Smith, K. Frameless stereotaxy and anterior cervical surgery. *Computer Aided Surgery* **4**(6): 322-327, 1999.

[16] Gong, J., Bächler, R., Sati, M., and Nolte, L.P. Restricted surface matching, a new approach to registration in computer assisted surgery. *Proc of CVRMed-MRCAS, Lecture Notes in Computer Science*, Springer, pp 597--605, 1997.

[17] Germano, I.M., and Queenan, J.V. Clinical experience with intracranial brain needle biopsy using frameless surgical navigation. *Computer Aided Surgery* **3**(1): 33--39, 1998.

[18] Schemerber, S., and Chassat, F. Accuracy evaluation of a CAS system: Laboratory protocol and results with 6D localizers, and clinical experiences in otorhinolaryngology. *Computer Aided Surgery* 13(1): 1-6, 2001.

[19] Simon, D.A., Jaramaz, B., Blackwell, M., et al. Development and validation of a navigational guidance system for acetabular implant placement. *Proc of CVRMe-MRCAS, Lecture Notes in Computer Science*. Springer, pp 597--605, 1997.

[20] Adler. J.R., Murphy, M.J., S.D. Chang, and S.L. Hancock. Image-guided robotic radiosurgery. *Neurosurgery* **44**(6): 1299—1307, 1999.

[21] Villalobos, H., and Germano, I.M. Clinical evaluation of multimodality registration in frameless stereotaxy. *Computer Aided Surgery* **4**(1): 45-49, 1999.

[22] Guéziec, A., Kazanzides, P., Williamson, B., and Taylor, R.H. Anatomy based registration of ct-scan and intraoperative X-ray images for guiding a surgical robot. *IEEE Transactions on Medical Imaging*. Special Issue on Image Guidance of Therapy, 1998.

[23] Hamadeh, A., Lavallée, S., and Cinquin, P., Automated 3-dimensional computed tomographic and fluoroscopic image registration. Computer Aided Surgery **3**(1), 1998.

[24] Hamadeh, A., Sautot, P., Lavallée, S., Cinquin, P. Towards automatic registration between CT and X-ray images: cooperation between 3D/2D registration and 2D edge detection. *Medical robotics and computer assisted surgery*, pp 39--46. Wiley, 1995.

[25] Lavallée, S., Szeliski, R., and Brunie, L. Anatomy-based registration of 3D medical images, X-ray projections, and 3D models using octree-splines. In Taylor R. H., Lavallée S., Burdea G. C., and Mösges R., editors, *Computer-integrated surgery: technology and clinical applications*. Chapter 7, pp 115--143. MIT Press, Cambridge MA, 1995.

[26] Tang, T.S.Y. Calibratrion and point based registration of fluoroscopic images. Master's Thesis, Department of Computing and Information Science, Queen's University, Kingston, Ontario, Canada, 1999.

[27] LaRose, D., Iterative X-ray/CT registration using accelerated volume rendering. PhD Thesis, Robotics Institute, Carnegie Mellon University. Pittsburgh, PA, May 2001.

[28] Lemieux, L., Jagoe, R., Fish, D.R., Kitchen, N.D., and Thomas, G.T. A patient-to-computed-tomography image registration method based on digitally reconstructed radiographs. *Medical Physics* **21**(11): 1749--1760, 1994.

[29] Murphy, M.J. An automatic six-degree-of-freedom registration algorithm for image-guided frameless stereotaxic radiosurgery. *Medical Physics* **24**(6):857--866, 1997.

[30] Penney, G.P., Weese, J., Little, J.A. et al. A comparison of similarity measures for use in 2D-3D medical image registration. *IEEE Transactions on Medical Imaging* **17**: 586-595, 1998.

[31] Roth, M., Brack, C. et al. Multi-view contour less registration of bone structures using a single calibrated x-ray fluoroscope. *Proc. of the 14th Int. Conf on Computer Aided Radiology and Surgery*, H.U. Lemke et al., editors, Elsevier, pp 756--761, 1999.

[32] Pluim, J.P., Maintz, J.B.A., and Viergever, M.A. Image registration by maximization of combined mutual information and gradient information. In S. L. Delp, A. M. DiGioia, and B Jaramaz, editors, *Medical Image Computing and Computer Assisted Intervention*. Springer, 2000.

[33] Yaniv, Z. Fluoroscopic X-ray image processing and registration for computer-aided orthopedic surgery. Master Thesis, Institute of Computer Science, The Hebrew University of Jerusalem, 1998.

[34] Brack, C., Burghart, R., Czpof, A. et al. Accurate X-ray navigation in computer-assisted surgery. *Proc. of the 12th Int. Symp. On Computer Assisted Radiology and Surgery*. H.U. Lemke et al., editors. Springer, 1998.

[35] Schreiner, S., Funda, J., Barnes, A.C., and Anderson, J.H. Accuracy assessment of a clinical biplane fluoroscope for three-dimensional measurements and targeting. In *Proc. of SPIE Medical Imaging*, 1995.

[36] Faugeras, O. *Three-Dimensional Computer Vision: A Geometric Viewpoint*. MIT Press, 1993.

[37] Tsai, R., A versatile camera calibration technique for high-accuracy 3D machine vision metrology using off-the-shelf tv cameras and lenses. *IEEE Transactions on Robotics and Automation*, **RA-3**(4), August 1987.

[38] Fitzpatrick, J.M., West, J.B., and Maurer Jr., C.R. Predicting error in rigid-body, point-based registration. *IEEE Transactions on Medical Imaging* **17**(5): 694—702, 1998.

[39] Fitzpatrick, J.M. and West, J.B., The distribution of target registration error in rigid-body, point-based registration. *IEEE Transactions on Medical Imaging* **20**: 917-927, 2001.

[40] West, J.B. Predicting error in point-based registration. PhD thesis, Department of Computer Science Vanderbilt University, Nashville, Tennessee, USA, 2000.

[41] Pennec, X., and Thirion, J.P. A framework for uncertainty and validation of 3D registration methods based on points and frames. *International Journal on Computer Vision*, **25**(1): 203--229, 1997.

[42] Ellis, R.E., Fleet, D.J., Bryant, J.T., Rudan, J., and Fenton, P. A method for evaluating CT-based surgical registration. In Troccaz et al., editors, *Lecture Notes in Computer Science* 1205. Springer, 1997.

[43] Leavers, V.F. Which Hough transform? *Computer Vision, Graphics, and Image Processing: Image Understanding*, **58**(2): 250--264, 1993.

[44] Yaniv, Z, Joskowicz, L., Simkin, A, Garza-Jinich, M., and Milgrom C. Fluoroscopic image processing for computer-aided orthopaedic surgery. In *Medical Image Computing and Computer Assisted Intervention*, 1998.

FIGURES

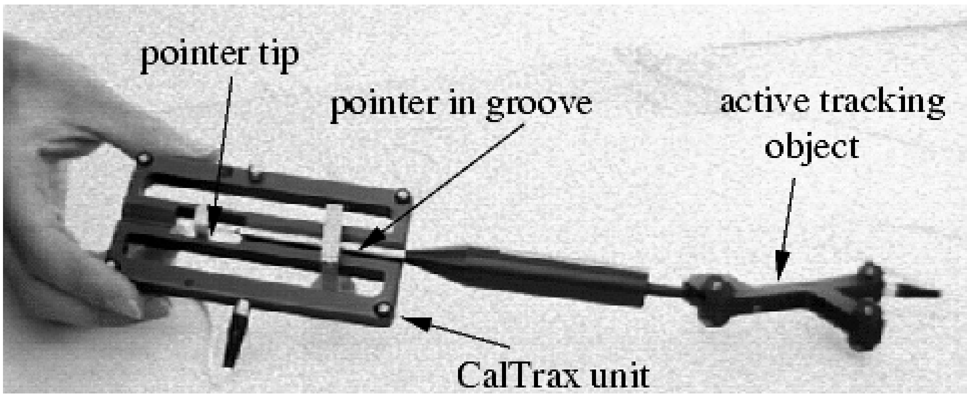

Figure 1: Photograph of the CalTrax unit calibrating an active pointer.

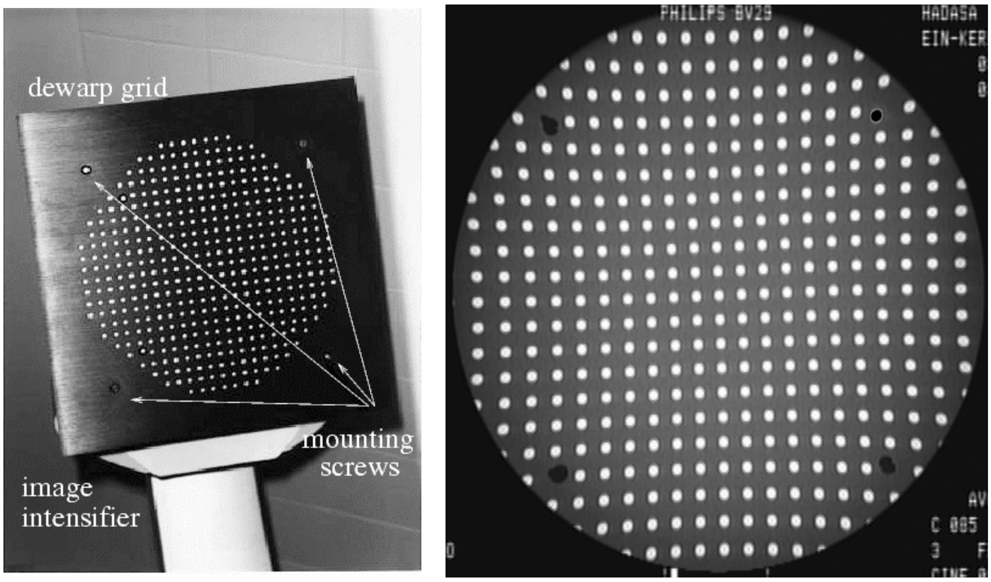

Figure 2: Dewarp grid on the C-arm image intensifier: (a) photograph, and (b) its fluoroscopic image.

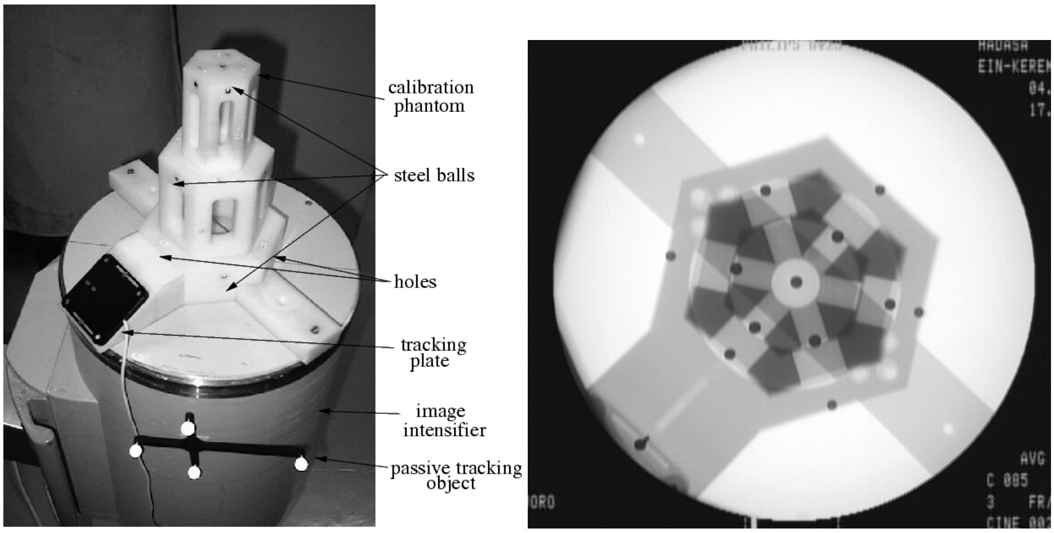

(a) (b)

Figure 3: Camera calibration tower on the C -arm image intensifier: (a) photograph, and (b) fluoroscopic image.

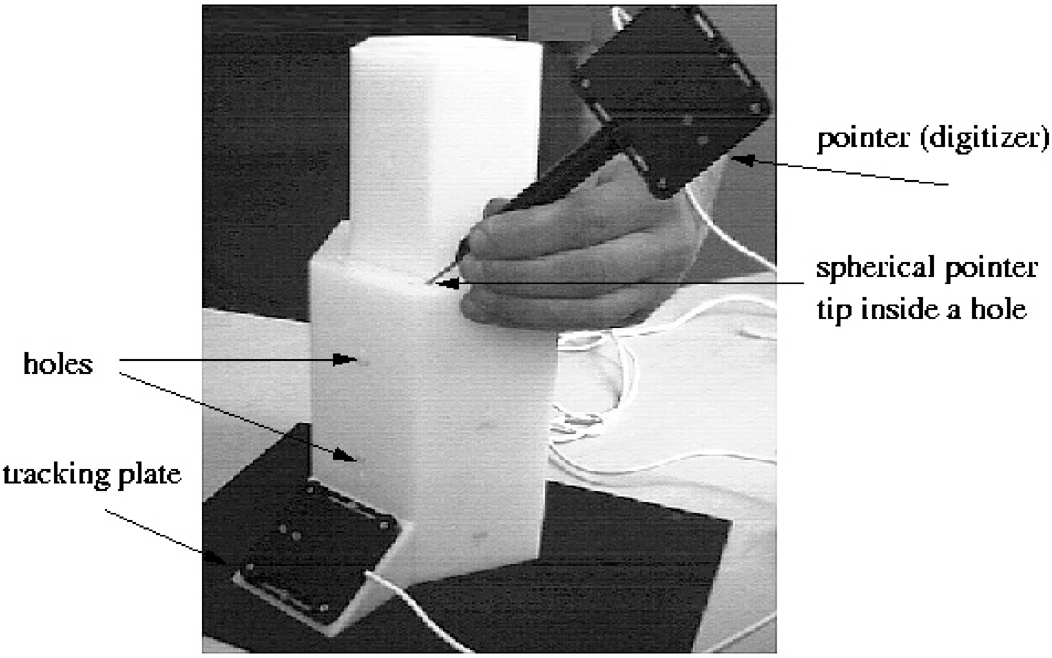

Figure 4: Photograph of the contact registration phantom with a pointer touching one of the holes on its side.

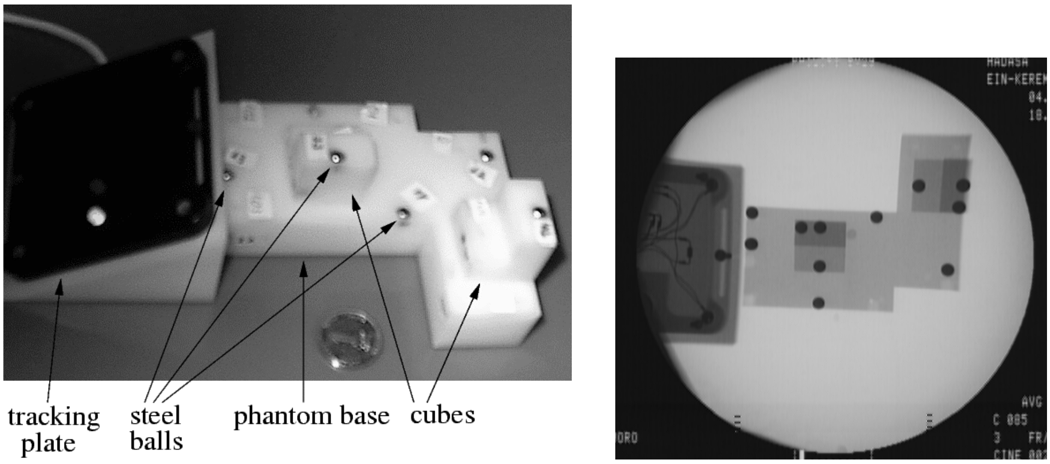

(a) (b)

Figure 5: Four-way registration phantom on a radiolucent table: (a) photograph and (b) fluoroscopic image from the top.

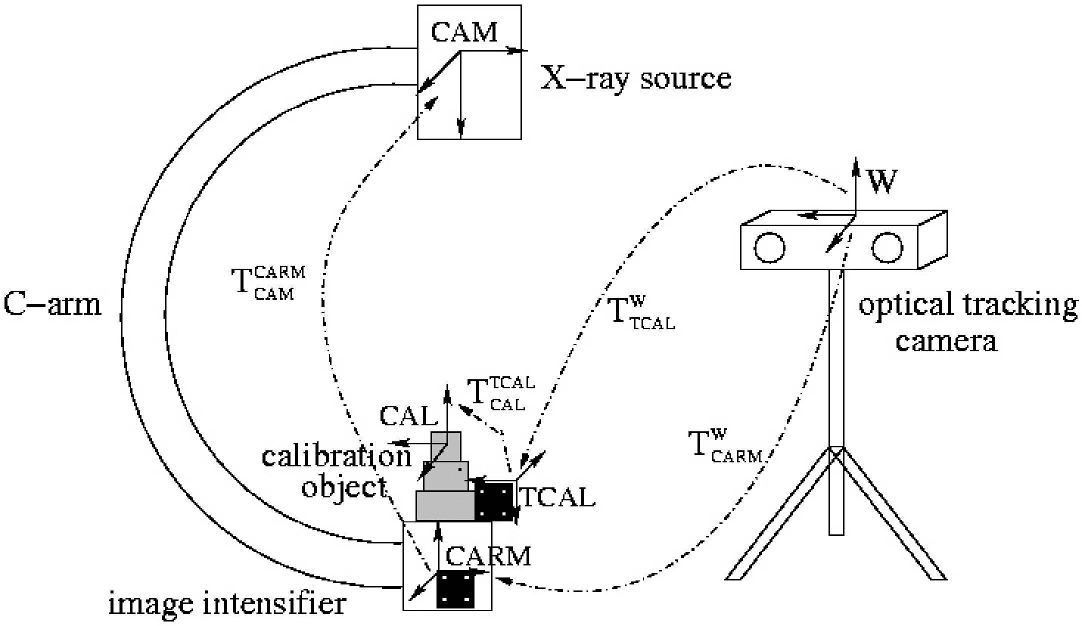

Figure 6: Schematic view of the C-arm calibration process. The coordinate systems are: *W*, the global coordinate system, which coincides with the tracker's coordinate system; *CARM*, the local coordinate system of the tracking unit attached to the C-arm's image intensifier; *CAL* the local coordinate system of the calibration object; *TCAL*, the local coordinate system of the tracking unit attached on the calibration phantom; *CAM*, the virtual coordinate system of the camera. The transformations between coordinate systems are: T_{CAM}^{CARM} camera and C-arm, T_{CAL}^{TCAL} between the calibration phantom and its tracking plate, T_{TCAL}^{W} between the phantom calibration plate and the world, and T_{CARM}^{W} between the C-arm and the world. The goal is to compute T_{CAM}^{CARM} and the internal camera parameters

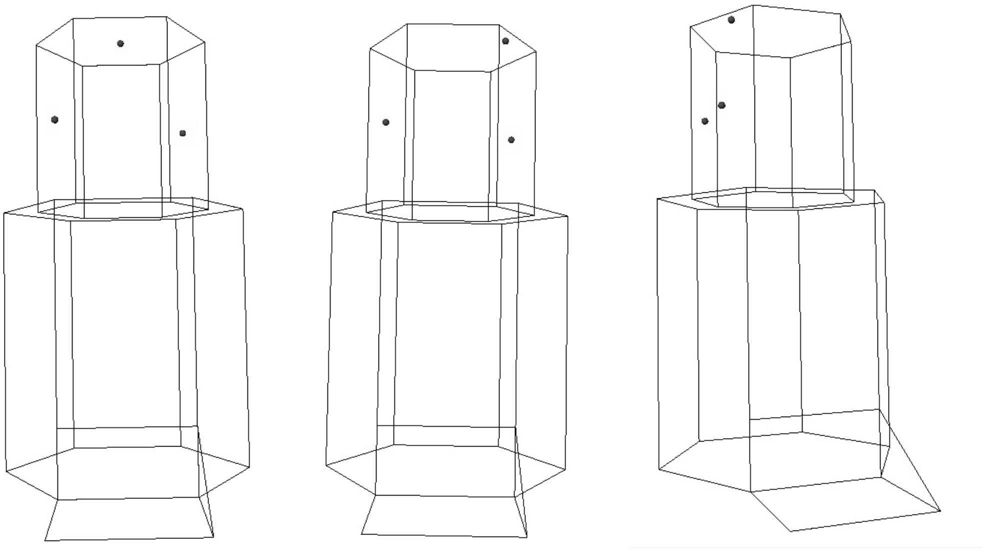

Figure 7: Three configurations of landmarks for contact-based registration with the contact registration phantom

TABLES

#	Mean	Std Dev	Max	Min
1	0.62	0.25	1.26	0.20
2	0.54	0.22	1.04	0.18
3	0.55	0.23	1.14	0.20
4	0.48	0.17	0.91	0.22
all	0.55	0.22	1.26	0.18

(a) TRE with five fiducials

#	Mean	Std Dev	Max	Min
1	0.44	0.23	0.98	0.12
2	0.46	0.21	1.14	0.18
3	0.49	0.34	1.49	0.10
4	0.67	0.33	1.36	0.09
all	0.51	0.29	1.49	0.09

(b) TRE with ten fiducials

Table 1: Results of contact-based landmark registration test (in mm): (a) target registration error with five fiducials, and; (b) target registration error with ten fiducials.

#	Mean	Std Dev	Max	Min
1	1.95	1.22	4.43	0.54
2	1.82	0,89	3.58	0.39
3	5.97	3.82	12.93	0.31
all	3.25	3.04	12.93	0.31

(a) landmarks with 2.5mm error

#	Mean	Std Dev	Max	Min
1	0.86	0.34	1.61	0.33
2	1.60	0.67	3.17	0.50
3	1.31	0.76	2.95	0.24
all	1.26	0.68	3.17	0.24

(b) landmarks + 15 point cloud

Table 2: Results of the contact-based registration experiment. (a) coarse registration with three landmarks with 2.5mm error in hole depth. (b) fine registration with cloud of 15 points and three landmarks with 2.5mm error. All errors are in millimeters.

Image	Camera angle	# of fiducials	Mean X shift	Mean Y shift	Mean Z shift	Mean	Std Dev	Max	Min
1	0^o	31	0.52	-0.04	-0.35	0.67	0.37	1.34	0.08
2	$+10^o$	32	0.21	-0.03	-0.20	0.71	0.35	1.35	0.09
3	-10^o	33	0.24	0.00	-0.98	1.12	0.79	2.68	0.14
4	0^o	32	0.15	-0.00	-0.42	0.83	0.42	1.77	0.12
1-4	all	128	0.28	-0.02	-0.49	0.84	0.54	2.68	0.08
5	0^o	36	0.05	0.00	-0.06	0.15	0.09	0.32	0.02

Table 3: Results of the first camera calibration accuracy experiment (all values except the C-arm camera angles in the second column are in millimeters). The first column and second columns show the image number and the camera angle. Columns 3 to 6 show the average fiducial center shift along each of the three directions relative to the closest point on the ray. The remaining columns show the distances of the fiducials from the closest point on the ray.

Image	Mean fiducial centers dist.	FOCAL DISTANCE		CENTER COORDINATES	
		setting 1	**setting 2**	**setting 1**	**setting 2**
1	0.07 (0.06)	969.12	955.80	X= -212.01 Y= -39.79 Z= 1073.25	X= 208.53 Y= 11.58 Z= -1063.49
2	0.06 (0.14)	963.73	953.03	X= 190.92 Y= 28.54 Z=-1074.14	X= -197.16 Y= -37.69 Z= 1063.83
3	0.10 (0.23)	964.02	951.12	X= 192.33 Y= 31.62 Z=-1074.06	X= 171.30 Y= 40.11 Z= -1066.53

Table 4: Results of the second camera calibration sensitivity experiment showing the sensitivity of computed camera parameters to noise in the fiducial detection algorithm. The first column is the image number. The second column shows the average distance in millimeters (pixels in parenthesis) between the detected fiducial on each image in two different settings. The next two columns show the computed camera focal distance (in mm) for each setting. The last two columns show the coordinates (in mm) of the projection center relative to the tracking unit on the C-arm.

Image #	**# of fiducials**	**Mean X**	**Mean Y**	**Mean Z**	**Mean**
1	12	0.01	< 0.01	< 0.01	0.05
2	12	< 0.01	< 0.01	0.04	0.05
3	11	0.03	< 0.01	0.02	0.06

Table 5: Results of the second camera calibration sensitivity test showing the actual effect of the change in camera parameters on the back projection process (all values are in mm). The X, Y, and Z values denote the differences between the closest points in the back projection process. The last column displays the mean distance between the closest points.

Registration base	**Mean shift**			**Std shift**			**distance**			
	X	***Y***	***Z***	***X***	***Y***	***Z***	***mean***	***std***	***max***	***min***
contact	0.18	0.27	-0.14	0.10	0.10	0.08	0.38	0.05	0.46	0.31
AP	1.72	-1.09	-6.06	0.41	0.24	0.11	6.41	0.08	6.51	6.29
Lateral	---	----	*F*	*A*	*I*	*L*	*E*	*D*	---	---
AP+lateral	1.68	-1.51	1.51	0.45	0.36	0.11	2.75	0.47	3.37	2.16

Table 6: Results of the image-based landmark registration test. Three computations of image based registration were made, two of them based on a single image (anterior/posterior (AP) and lateral) and one on both. Columns 2-4 show the mean shift of the phantom positional holes relative to the hole position computed from the registration matrix. Columns 5-7 show the standard deviation of this shift. Columns (8-11) show the mean, standard deviation, maximum, and minimum distance between these points (all values are in mm).

Data set / # of images	**Rotation variation**			**Translation variation**		
	X	***Y***	***Z***	***X***	***Y***	***Z***
Series 1						
one image	0.55	-0.23	1.05	-5.87	2.42	1.60
two images	1.11	0.10	1.57	-1.19	-0.23	1.66
three images	2.06	0.41	2.23	1.43	-2.22	1.45
mean	1.24	0.09	1.62	-1.88	-0.01	1.57
Series 2						
one image	0.08	0.21	0.67	-4.60	-4.15	1.72
two images	0.07	0.21	0.72	2.31	-0.66	1.60
mean	0.07	0.21	0.69	-1.14	-2.40	1.66
Relative values mean	0.77	0.14	1.25	-1.58	-0.97	1.61
Absolute values mean	0.77	0.23	1.25	3.08	1.94	1.61

Table 7: Results of the comparison between contact and image-based landmark registration test. The values are the difference between the transformation matrix rotation and translation parameters obtained with image-based landmark registration and those obtained with the contact-based landmark registration (rotation values are in degrees, translation values are in millimeters).